TECHNICAL PAPER

Failure criterion for SPIF based on mean stress

Rafael Gustavo Schreiber[1] · Ariton Araldi[1] · Maurício Kiniz Júnior[1] · Anderson Daleffe[2] · Lirio Schaeffer[3]

Abstract

In this paper, an analytical method was created to estimate single point incremental forming (SPIF)'s strain limits, based on mean stress calculated using membrane analysis. We conducted 27 formability experiments using different materials (SAE1008, AA1200-H14 and C268), different thicknesses and different tool radii values, followed by simulations of the finite element method (FEM) and analysis of variance (ANOVA). To validate the results obtained in these experiments, three FEM simulations were made. After the formability experiments, we were able to verify what effects the materials, the tool radii and the interaction between the two had on the stress value used as a failure criterion. The FEM simulations allowed us to validate analytical equations according to membrane equilibrium conditions, and the analytical method that considers the mean stress as critical stress presented good accuracy, with a maximum percentage error of 6.7%, compared to strain experimental values.

Keywords SPIF · Failure criterion · Mean stress · FEM

1 Introduction

The incremental sheet forming (ISF) process uses successive and localized strains to form material using movements from hemispherical tipped tools. This is a process that is easily made with CNC machines and can be applied to small production lots [1], as well as to prototype production and personalized products [2]. Among the ISF application areas, we can cite prosthetics [3–5], solar collectors [6–8], parts for the automobile industry [9–11] and aeronautic industry [12, 13].

Due to ISF's formation mechanism, with localized strain, it is possible to achieve greater strain levels before the appearance of fractures if compared to conventional sheet strain processes [2]. Strain limits to incremental sheet forming are expressed by fracture forming limit diagram (FFLD), which presents a formability limit line with a negative incline (angular coefficient of approximately -1) in the 1st quadrant of major strain φ_1's and minor strain φ_2's coordinate systems [14]. The formability trials used in ISF to define FFLD limits are the groove test [15–17] and the hyperboloid shape [18–21]. Do et al. [14] have defined a method for FFLD construction from the formation of three distinct shapes, with the objective of obtaining different types of strain. As a result, they have obtained a diagram with an angular coefficient close to -1 for all analyzed materials.

Several parameters present FFLD position influence for incremental sheet forming, such as material, thickness, tool radius, step-down, rotation speed and tool feed rate speed [22]. Micari [23] has developed a study to evaluate material property influence in ISF formability, verifying that the yield constant C and strain-hardening exponent n are parameters

✉ Rafael Gustavo Schreiber
   rafael.schreiber@ifsc.edu.br

   Ariton Araldi
   ariton.araldi@ifsc.edu.br

   Maurício Kiniz Júnior
   mkmk.junior@gmail.com

   Anderson Daleffe
   anderson.daleffe@satc.edu.br

   Lirio Schaeffer
   schaefer@ufrgs.br

1 Federal Institute of Education, Science and Technology of Santa Catarina (IFSC), Lages, SC 88506-400, Brazil

2 University Center UNISATC, Criciúma, SC 88805-380, Brazil

3 Federal University of Rio Grande Do Sul (UFRGS), Porto Alegre, RS 91501-970, Brazil

with greater influence over formability when compared to tensile strength, elongation and anisotropy.

Sheet thickness influence can be observed in the cosine law (Eq. 1) where s_0 is initial sheet thickness, s is final sheet thickness, and θ is wall angle [24, 25]. For a particular material, the greater the initial sheet thickness, the greater the formability, which can be represented both by the maximum wall angle [22] and by strain. The relation between wall angle and φ_3 thickness strain is expressed in Eq. 2 [26]. All symbols used in this work's equations are presented in Table 1.

$$s = s_0 \cos \theta \tag{1}$$

$$\varphi_3 = \ln \left(\frac{\pi}{2} - \theta \right) \tag{2}$$

In general, the use of a small tool radius can lead to an increase in material formability [8, 27]. According to Martins et al. [26], greater thickness and smaller tool radius can cause triaxial decrease, providing a more stable strain mechanism and, along with it, an increase in formability. However, Al-Ghamdi and Hussain [24] have defined the relation of $R_t \approx 2.2 s_0$ as a relation value between tool radius (R_t) and initial sheet thickness (s_0) in order to obtain greater formability, since smaller radii (below this relation) can make the strain unstable, reducing formability.

Several studies were developed to try and establish ISF failure criteria, using analytic methods based on ductile

damage models. Han and Kim [28] have developed a failure criterion based on the Cockroft–Latham damage model and on the maximum shear stress and have applied it in experiments with steel and aluminum sheets. Huang et al. [29] have developed a failure criterion based on the Oyane model, considering wall angle, initial sheet thickness, step-down, tool radius and two constants, which they then applied in experiments using AA5052-O.

Gatea et al. [27] have developed a modified Gurson–Tvergaard–Needleman (GTN) damage criterion, considering the triaxiality to predict ductile fracture in the ISF process of pure titanium (grades 1 and 2). Silva et al. [30] have used an Ayada damage model, based on triaxiality, to define a damage equation that can be used according to tool radius and final sheet thickness to predict FFLD material position, regardless of strain state. Wu et al. [31] have developed a damage criterion based on triaxiality and process parameters, such as tool radius, final thickness and wall angle, and have applied it to AA1050-H111.

Triaxiality plays an important role in the fracture mechanism in SPIF. However, in incremental sheet forming, the triaxiality is lower if compared to the conventional processes, which allows to apply greater strains to the material [26] Since the mean stress is a parameter related to triaxiality, this can be a good indicator of failure, mainly because it is easy to calculate.

The present work has as its objective to present an analytical method using mean stress value, calculated using membrane analysis [30], as a reference parameter to determine the strain limit in single point incremental forming (SPIF) applied to different materials.

2 Materials and methods

In this study, 27 experiments of hyperboloid formability through single point incremental forming were conducted in different materials, tool radii and thicknesses. After that, three FEM simulations were made to validate the measured and calculated results of the experiments. And finally, an ANOVA analysis of variance was conducted to determine how significant each strain limit parameter was. Based on these data, a method was determined to estimate the strain limit of the material according to the mean stress critical value.

2.1 SPIF experiments

Formability experiments consisted in single point incremental forming of 27 sheets in hyperboloid format, varying parameters of material, tool radius ($R_t = 3$, 5 and 7.5 mm) and initial sheet thickness. The materials used in this study were SAE1008 steel, AA1200-H14 aluminum and C268

Table 1 Parameters

Symbol	Parameter	Unit
C	Yield Constant	MPa
h	Maximum deep	mm
n	Strain-hardening Exponent	–
R_t	Tool radius	mm
s	Final thickness	mm
s_0	Initial thickness	mm
Δz	Step-down	mm
φ_1	Major strain	–
φ_2	Minor strain	–
φ_3	Thickness strain	–
φ_{eq}	Equivalent strain	–
σ_1	Maximum principal stress	MPa
σ_2	Intermediate principal stress	MPa
σ_3	Minimum principal stress	MPa
σ_c	Critical stress	MPa
σ_{eq}	Equivalent stress	MPa
σ_m	Mean stress	MPa
θ	Final wall angle	rad
θ_0	Initial wall angle	rad

Table 2 Material properties

Material	Initial thickness, s_0 (mm)	Yield strength (MPa)	Tensile strength (MPa)	Elongation (%)	Modulus of elasticity (GPa)	Yield constant, C (MPa)	Strain-hardening exponent, n (−)
SAE1008	0.60/0.75/0.90	265	359	41.5	190	619.86	0.2163
AA1200-H14	0.50/0.80/1.20	97	117	3.6	70	181.45	0.1080
C268	0.50/0.81/1.06	296	413	37.5	105	734.28	0.2624
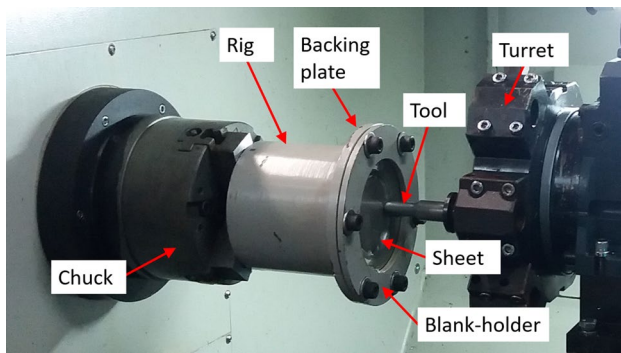
Fig. 1 SPIF process being performed at the CNC lathe

brass. Initial sheet thicknesses, as well as properties of the materials used in this work, are available in Table 2.

The mechanical properties of the materials indicated in Table 2 were obtained from the literature (from the tensile test), based on the studies by Haag and Ferranti [32] for SAE1008 steel, Schreiber et al. [8] for AA1200-H14 aluminum and Maximiliano et al. [33] for C268 brass.

All experiments were conducted until a material fracture could be identified. By the end of the process, strains were evaluated and final thickness was calculated, as well as the stress values in each experiment.

The experiments were conducted in a Nardini brand CNC lathe, model LOGIC 195VS. The sheet was fixed by a set made out of blank-holder, backing plate and rig, which were moved by the chuck, while the tool was led by the machine's turret, as shown in Fig. 1. Although the lathe can only manufacture cylindrical parts, it met the requirements of this work, since the shape of the parts used in the experiments is cylindrical.

The formed format of each experiment was the hyperboloid, with dimensions presented in Fig. 2a. This format allows each tool's step-down over the sheet to be formed at a new wall angle, so as to gradually increase the angle from θ_0 to θ, while the initial thickness s_0 decreases until the final thickness s and a fracture occurs on the sheet at a maximum h depth.

Figure 2b presents the tool path during the experiments. Considering that the turret's linear trajectories were made by tool dislocation (with a feed rate of 100 mm/min), while circular trajectories were made by chuck rotation (with rotation speed of 2 rpm). All experiments were conducted with a step-down value of $\Delta z = 1$ mm and without tool rotation
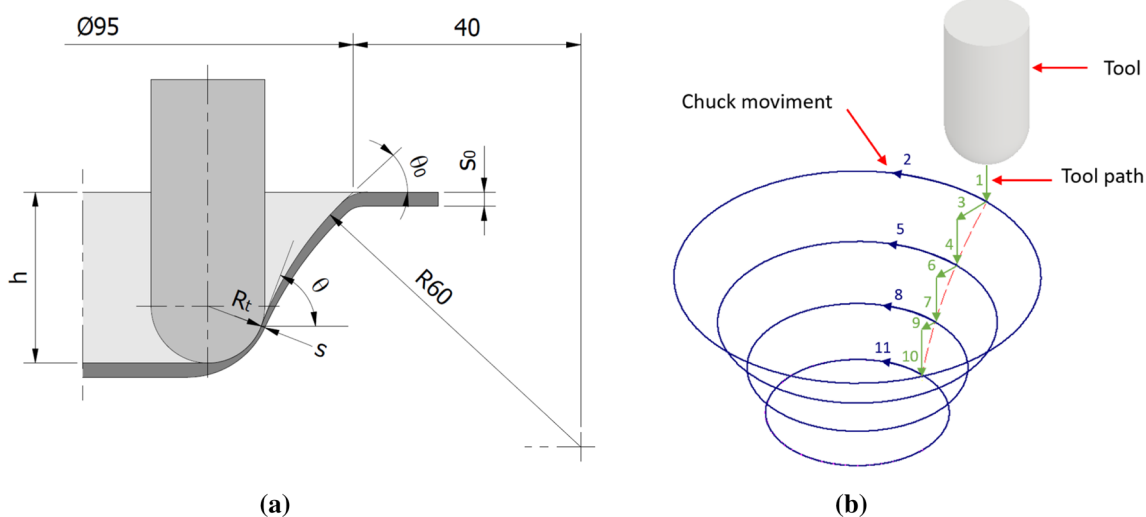
Fig. 2 **a** Shape formed in the SPIF experiments, **b** tool path on experiments

movement. We decided to use the step path in the experiments because it has low strain limits. And thus, with this tool path, we were able to obtain more severe stress concentration conditions than it would have been able with a helical path, for example.

For these experiments, it was necessary to use three hemispherical tipped tools (with different radii), considering that they were all fabricated with quenched and tempered SAE 1045 steel. For lubrication during the process, before the beginning of each experiment, a thin layer (5 ml) of VG100 oil was deposited using a pipette over the surface to be formed.

The strain analysis obtained from each formed sheet was made through the use of electrochemical recording in a circular grade over the sheets, with initial dimension of $d_0 = 1$ mm. After the strain, the circles changed into ellipses, and these ellipses were used to measure and determine the strains that occurred (Fig. 3). The major strain φ_1 is calculated using Eq. 3, where d refers to the length of the final ellipses.
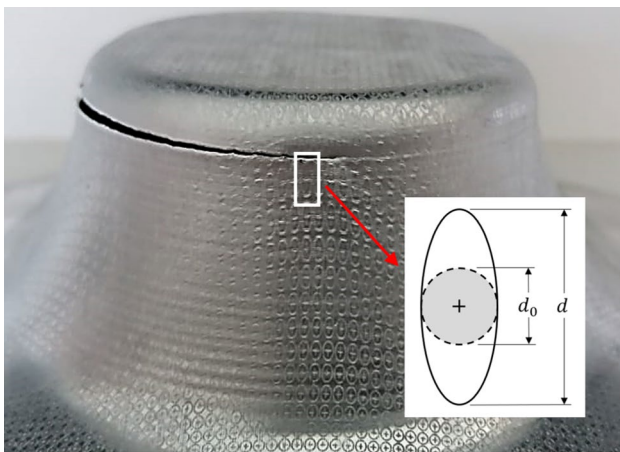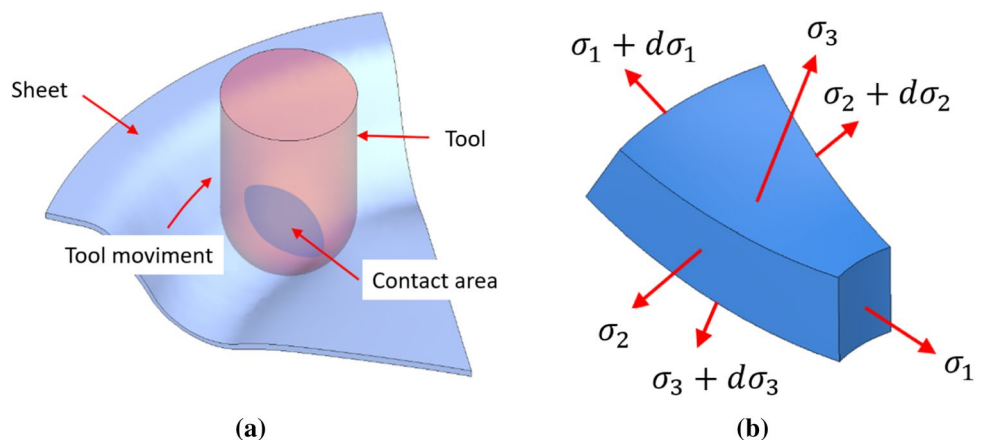

Fig. 3 Strain determination method

$$\varphi_1 = \ln\left(\frac{d}{d_0}\right) \tag{3}$$

In the case of the hyperboloid, we obtained a plane strain state, where the minor strain $\varphi_2 = 0$ and the thickness strain are defined as $\varphi_3 = -\varphi_1$ (according to volume consistency). The final thickness was estimated according to thickness strain, as indicated in Eq. 4. Whereas the final wall angle θ is calculated by Eq. 5, according to thickness strain as well.

$$s = s_0 e^{\varphi_3} \tag{4}$$

$$\theta = \frac{\pi}{2} - e^{\varphi_3} \tag{5}$$

The von Mises equivalent strain in each experiment is calculated by Eq. 6, and for the plane strain state, it is simplified by Eq. 7.

$$\varphi_{eq} = \frac{\sqrt{2}}{3}\sqrt{(\varphi_1 - \varphi_2)^2 + (\varphi_2 - \varphi_3)^2 + (\varphi_3 - \varphi_1)^2} \tag{6}$$

$$\varphi_{eq} = \frac{2\sqrt{3}}{3}|\varphi_3| \tag{7}$$

The equivalent stress (σ_{eq}) was determined according to material properties and to equivalent strain, as expressed in Eq. 8 (Ludwik–Hollomon equation).

$$\sigma_{eq} = C\varphi_{eq}^n \tag{8}$$

Considering that the contact area between the sheet and the tool is submitted to the principal stress coming from three directions (Fig. 4a), those being: maximum principal stress (σ_1), intermediate principal stress (σ_2) and minimum principal stress (σ_3), as indicated in the volume element of the sheet under the contact area (Fig. 4b).

Fig. 4 a Contact area between tool and sheet during the SPIF process, **b** principal strains in the sheet's volume element

(a)

(b)

For the plane strain state, the principal stress (using the von Mises criterion) is calculated by Eqs. 9–11, and mean stress (σ_m) is calculated by Eq. 12 [34]. These equations follow the simplifications imposed by membrane equilibrium conditions, that is, they disregard bending moments, as well as the material's strain hardening and anisotropy effects. Furthermore, they assume axial symmetry and that the friction is small, considering that the frictional stress is constituted by a meridional component and another circumferential component in the plane [30].

$$\sigma_1 = \frac{2\sigma_{eq}}{\sqrt{3}} \left(\frac{R_t}{R_t + s} \right) \tag{9}$$

$$\sigma_2 = \frac{\sigma_{eq}}{\sqrt{3}} \left(\frac{R_t - s}{R_t + s} \right) \tag{10}$$

$$\sigma_3 = -\frac{2\sigma_{eq}}{\sqrt{3}} \left(\frac{s}{R_t + s} \right) \tag{11}$$

$$\sigma_m = \frac{1}{3}\left(\sigma_1 + \sigma_2 + \sigma_3\right) = \frac{\sigma_{eq}}{\sqrt{3}} \left(\frac{R_t - s}{R_t + s} \right) \tag{12}$$

In order to evaluate the effects of material, tool radius and thickness parameters in the critical stress results obtained in each experiment, an ANOVA analysis of variance was made. To determine if the data obtained were parametric, a Shapiro–Wilk test was performed (to evaluate normalcy), as well as a Levene test (to evaluate variance homogeneity).

In order to compare different combinations of the groups analyzed, the ANOVA was followed by the Bonferroni post hoc test. The statistical analysis was made using RStudio software, and the $p < 0.05$ value was used as a criterion of statistical significance in the analysis.

2.2 FEM simulation

The finite elements method (FEM) was conducted to validate the final thickness and mean stress values obtained in the SPIF experiments. In order to do that, three simulations were made reproducing the conditions of experiments 7, 16 and 25. FEM simulations were made with Simufact Forming software in the Sheet Metal Forming module, using the 3D simulation type and with a solid-shell type element. The tool, the blank-holder, the backing plate and the sheet were modeled to make the hyperboloid formation with the same depth obtained in each experiment. However, to decrease the simulation time, the initial diameter of the hyperboloid was reduced in the simulation model.

The tool paths were configured by tabular motion using the time calculated for each path as a feed rate tool function in the experiments (100 mm/min) and the chuck rotation speed (2 rpm). The sheet's and tools' temperatures were kept constant at 20 °C. And the friction coefficient selected was 0.1, following the Coulomb law.

The sheet's material was configured as C268 brass with initial thickness of 0.50 mm (with mechanical properties indicated in Table 1). Solid-shell-type elements were selected for the sheet. The sheet's mesh was created with the element's edge length set at 1.0 mm. A refinement box was defined with the element's edge length mesh dimensions set at 0.25 mm, according to the region indicated in Fig. 5, which corresponds to the tool movement location at the Z-axis. The tool's radii used in each simulation were 7.5, 5 and 3 mm, as they were in the experiments.

The analytical method, used to calculate the stresses in the experiments (Table 3), follows simplifications from the membrane equilibrium conditions, which disregard the anisotropy of the material. Because of this, in these simulations, the material was considered isotropic, in order to compare its results with the calculated values.

A calculation of percentage error (Eq. 13) was used to compare the final sheet thickness and mean stress values obtained in the simulations in relation to the values obtained

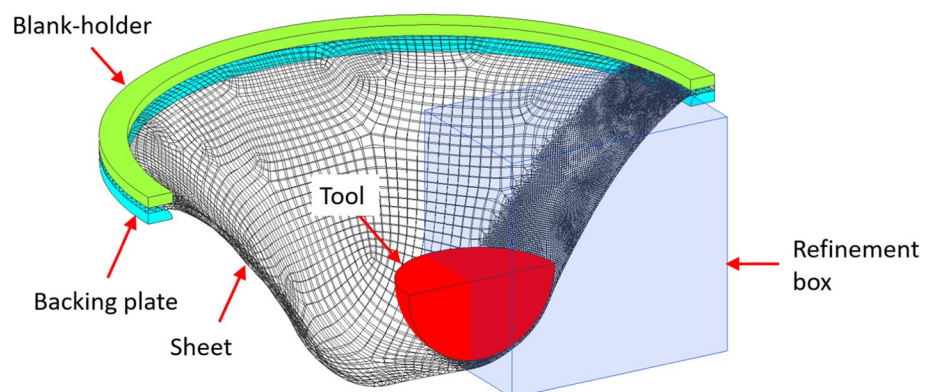**Fig. 5** Assembly of ISF test to FEM

Table 3 Results of SPIF formability experiments

Exp	Material	R_t (mm)	s_0 (mm)	s (mm)	θ (°)	φ_1 (−)	φ_2 (−)	φ_3 (−)	φ_{eq} (−)	σ_1 (MPa)	σ_2 (MPa)	σ_3 (MPa)	σ_{eq} (MPa)	σ_m (MPa)
1	SAE1008	7.5	0.60	0.182	72.6	1.192	0.000	−1.192	1.376	748.8	365.3	−18.2	664.2	365.3
2	SAE1008	7.5	0.75	0.217	73.4	1.240	0.000	−1.240	1.432	751.8	365.0	−21.8	669.9	365.0
3	SAE1008	7.5	0.90	0.260	73.4	1.240	0.000	−1.240	1.432	747.6	360.8	−26.0	669.9	360.8
4	AA1200-H14	7.5	0.50	0.160	71.7	1.141	0.000	−1.141	1.318	211.4	103.4	−4.5	186.9	103.4
5	AA1200-H14	7.5	0.80	0.203	75.5	1.373	0.000	−1.373	1.585	214.4	104.3	−5.8	190.7	104.3
6	AA1200-H14	7.5	1.20	0.252	78.0	1.562	0.000	−1.562	1.804	216.1	104.4	−7.2	193.4	104.4
7	C268	7.5	0.50	0.202	66.8	0.906	0.000	−0.906	1.046	835.4	406.5	−22.5	743.0	406.5
8	C268	7.5	0.81	0.289	69.5	1.030	0.000	−1.030	1.189	854.3	410.7	−32.9	768.4	410.7
9	C268	7.5	1.06	0.357	70.7	1.087	0.000	−1.087	1.255	858.9	409.0	−40.9	779.3	409.0
10	SAE1008	5.0	0.60	0.170	73.8	1.264	0.000	−1.264	1.460	751.3	362.9	−25.5	672.7	362.9
11	SAE1008	5.0	0.75	0.203	74.5	1.309	0.000	−1.309	1.512	752.2	360.9	−30.5	677.8	360.9
12	SAE1008	5.0	0.90	0.238	74.9	1.331	0.000	−1.331	1.537	749.8	357.1	−35.7	680.2	357.1
13	AA1200-H14	5.0	0.50	0.160	71.7	1.141	0.000	−1.141	1.318	209.2	101.2	−6.7	186.9	101.2
14	AA1200-H14	5.0	0.80	0.207	75.2	1.352	0.000	−1.352	1.561	211.1	101.2	−8.7	190.4	101.2
15	AA1200-H14	5.0	1.20	0.286	76.3	1.434	0.000	−1.434	1.656	209.3	98.7	−12.0	191.6	98.7
16	C268	5.0	0.50	0.196	67.6	0.938	0.000	−0.938	1.083	833.2	400.3	−32.6	749.8	400.3
17	C268	5.0	0.81	0.281	70.1	1.059	0.000	−1.059	1.223	846.2	399.3	−47.5	774.0	399.3
18	C268	5.0	1.06	0.339	71.7	1.141	0.000	−1.141	1.318	853.5	397.9	−57.8	789.2	397.9
19	SAE1008	3.0	0.60	0.182	72.6	1.192	0.000	−1.192	1.376	723.1	339.6	−43.9	664.2	339.6
20	SAE1008	3.0	0.75	0.198	74.9	1.331	0.000	−1.331	1.537	736.8	344.1	−48.7	680.2	344.1
21	SAE1008	3.0	0.90	0.219	76.1	1.414	0.000	−1.414	1.633	741.7	343.8	−54.1	689.2	343.8
22	AA1200-H14	3.0	0.50	0.160	71.7	1.141	0.000	−1.141	1.318	204.9	97.0	−10.9	186.9	97.0
23	AA1200-H14	3.0	0.80	0.180	77.1	1.491	0.000	−1.491	1.722	209.6	98.5	−12.6	192.4	98.5
24	AA1200-H14	3.0	1.20	0.225	79.3	1.674	0.000	−1.674	1.933	209.3	96.8	−15.7	194.8	96.8
25	C268	3.0	0.50	0.233	63.3	0.764	0.000	−0.764	0.882	761.4	351.1	−59.1	710.6	351.1
26	C268	3.0	0.81	0.307	68.3	0.970	0.000	−0.970	1.120	792.3	355.6	−81.1	756.4	355.6
27	C268	3.0	1.06	0.368	70.1	1.059	0.000	−1.059	1.223	796.2	349.3	−97.6	774.0	349.3

in the experiments, where X refers to the data obtained in the simulations, and X_{exp} refers to the data calculated from the experiment's results.

$$\text{Percentage error} = \frac{\left|X - X_{exp}\right|}{X_{exp}} 100 \qquad (13)$$

3 Results and discussion

3.1 SPIF experimental results

Table 3 is filled in accordance with the 27 SPIF formability experiments, with the entry parameters: tool radius, material and initial thickness. It also shows the results of final thickness, final angle, strain and stress.

In order to use the failure criterion based on stress, the nomenclature that was established was "critical stress" (σ_c), used to describe the mean stress (Table 3), which was used to identify the fracture in each experiment.

The three-way ANOVA (Material $\times R_t \times s_0$) has shown that there is no effect in initial thickness or in its interactions with the other parameters in regards to critical stress values. Although the sheet's initial thickness may be an influent formability parameter [22, 24], as indicated in the cosine law (Eq. 1). It was observed that the fracture on the material occurred with critical stress values independent from the sheet's initial thickness.

Afterward, a two-way ANOVA (Material $\times R_t$) model was created, which has shown significant effect on the material [F (2, 18) = 48,310.29; $p < 0.001$], on the tool radius [F (2, 18) = 436.97; $p < 0.001$], and on the interaction between material and tool radius [F (4, 18) = 128.89; $p < 0.001$] at

the critical stress value. The Shapiro–Wilk and Levene tests indicated normalcy in the residue and homogeneity in the variances.

Post hoc (Bonferroni) analysis has shown that the critical stress value is dependent on material, as expected. Post hoc analysis has also shown that critical stress is dependent on tool radius on brass, in all comparisons. However, the radius is not dependent for steel between 5 and 7.5 mm. And on aluminum, the critical stress only showed dependency on tool radius between 3 and 7.5 mm.

Figure 6 presents a chart of the interaction between the parameters evaluated in the two-way ANOVA, where it is possible to see that the tool radius' influence on the critical stress on brass and steel is more accentuated than on aluminum.

Since C and n parameters, as well as tensile strength, vary significantly between the materials used in this study (Table 2), we had already expected that the material would have an effect on critical stress, as it does on formability [23].

And since the tool radius has its effect over formability explained in regard to triaxiality [26], it was also expected that it would have an effect over critical stress. However, we found that this effect was not equal in all materials in the same way.

3.2 FEM results

After the three experiments' FEM simulations, we were able to identify the critical point, where an accentuated reduction in the sheet's thickness occurs during the experiment and its consequent fracture. Figure 7 indicates the critical point in the simulation corresponding to experiment 25, within the

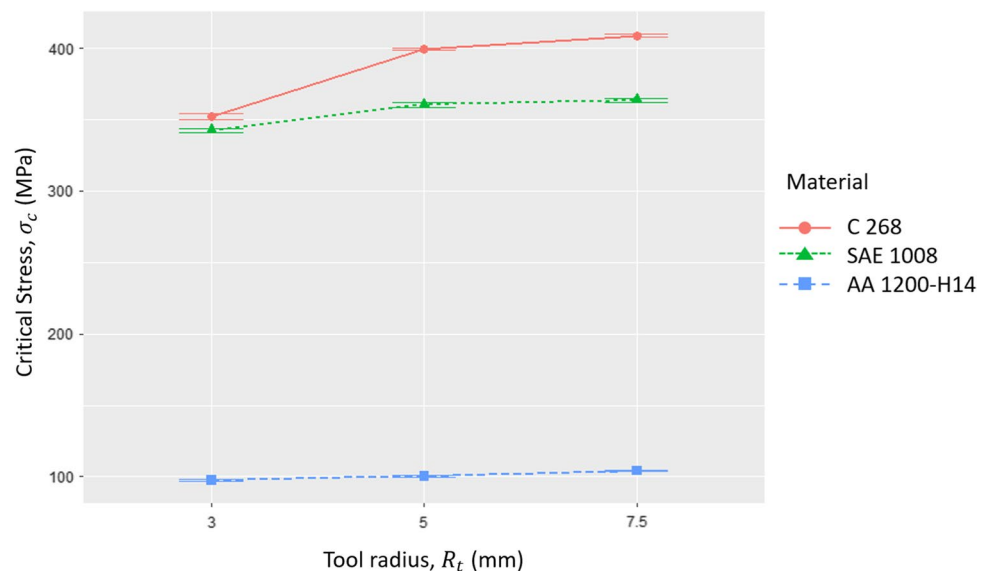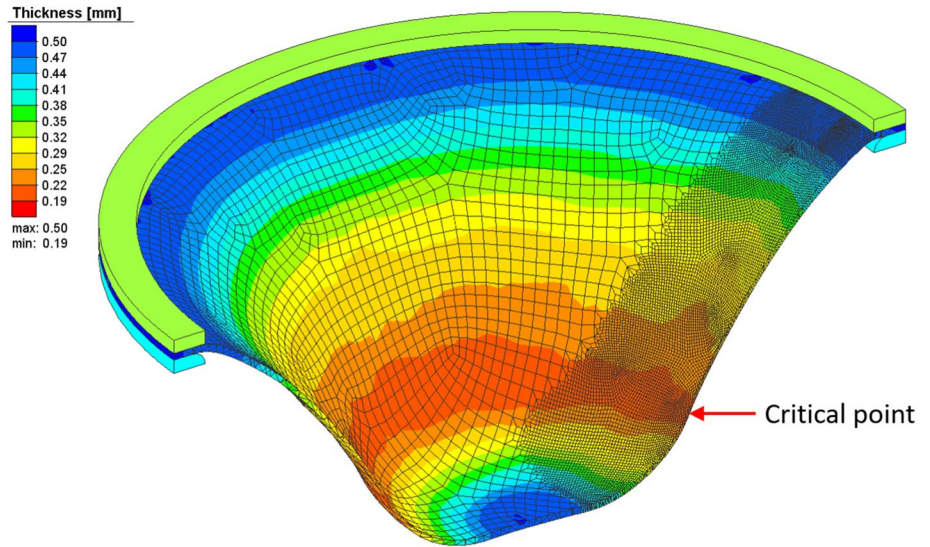**Fig. 6** Effects of Rt and material values under critical stress

Fig. 7 FEM simulation to Exp. 25—Thickness results

refinement box. At this location, we measured the thickness, and also, the mean stress values found in each simulation.

Table 4 shows a comparison between the calculated data using the experimental results and the data obtained by the FEM simulation, indicating the error percentage for each comparison. The thickness percentage error varied between 3.6 and 6%, while mean stress error varied between 1.9 and 4.2%. This percentage error is slightly smaller than that obtained in the studies by Jalali et al. [35], which reached 7% between the strain values obtained by FEM in relation to SPIF experiments. As such, it is possible to conclude that the thickness and mean stress data obtained through analytical method in the experiments are consistent with the data provided by the FEM simulation.

The three simulations were performed for the same material (C268 brass). As the values obtained for this material were very close to the experimental values, it is to be expected that the same will occur for the other materials, since the mean stress and the final thickness are proportional to the strain.

The fracture location (critical point in Fig. 7) is in accordance with the experiments conducted in this work (Fig. 3), as well as with the results from the experiments and the FEM simulations obtained in other studies [21, 27], which also describe this location as the one with greater stress and a more accentuated reduction in thickness for the hyperboloid shape. In the studies by Tayebi et al. [36] on the manufacturing of

pieces in the shape of a truncated cone, the authors have found that when the wall angle exceeds the limiting angle, the fracture occurs in the same position as indicated in this work.

3.3 Method development

Considering the mean stress (Table 3) as "critical stress," it is possible to establish this value as the failure criterion in SPIF, as indicated in Eq. 14 (applied to the plane state of strains $\varphi_2 = 0$).

$$\sigma_c = \sigma_m = \frac{\sigma_{eq}}{\sqrt{3}} \left(\frac{R_t - s}{R_t + s} \right) \tag{14}$$

According to this failure criterion based on critical stress, we were able to deduce Eqs. 14, 15, 16, to be used as an iterative method to predict maximum wall angle θ (Eq. 15), thickness strain φ_3 (Eq. 16) or major strain φ_1 (Eq. 17), for each process condition.

$$\sigma_c = \frac{C}{\sqrt{3}} \left(\frac{R_t - s_0 \cos\theta}{R_t + s_0 \cos\theta} \right) \left[\frac{2\sqrt{3}}{3} \left| \ln\left(\frac{\pi}{2} - \theta\right) \right| \right]^n \tag{15}$$

$$\sigma_c = \frac{C}{\sqrt{3}} \left(\frac{R_t - s_0 e^{\varphi_3}}{R_t + s_0 e^{\varphi_3}} \right) \left(\frac{2\sqrt{3}}{3} |\varphi_3| \right)^n \tag{16}$$

Table 4 FEM results

Exp	Experimental outputs		FEM model predicted outputs		Percentage error	
	s (mm)	σ_m (MPa)	s (mm)	σ_m (MPa)	in s (%)	in σ_m (%)
7	0.202	406.5	0.211	398.8	4.5	1.9
16	0.196	400.3	0.203	411.7	3.6	2.8
25	0.233	351.1	0.219	366.0	6.0	4.2

$$\sigma_c = \frac{C}{\sqrt{3}}\left(\frac{R_t - s_0 e^{(-\varphi_1)}}{R_t + s_0 e^{(-\varphi_1)}}\right)\left(\frac{2\sqrt{3}}{3}\varphi_1\right)^n \tag{17}$$

Equation 15, used to determine wall angle, is obtained by substituting Eqs. 1, 2 and 8 in Eq. 14. While Eq. 16, regarding thickness strain, is obtained by substituting Eqs. 4, 7 and 8 in Eq. 14. Equation 17 is useful to obtain strain limits in graphic format through FFLD, it is obtained from Eq. 16, considering $\varphi_3 = -\varphi_1$ as the plane state of strain.

Using this method, knowing the critical stress value that results from the fracture in the material (in the plane state of strain) and selecting data on the material (C, n and s_0), as well as tool radius (R_t), it is possible to estimate the maximum wall angle, the maximum strain and, furthermore, to define the FFLD position for the strain condition.

Based on the results of the statistical analysis, the critical stress value was determined according to material and tool radius. Table 5 shows mean values of critical stress for each material and tool radius, regardless of the sheets' initial thicknesses.

To validate the analytical method presented in this work, we compared the experimental major strain values with the major strain values calculated using Eq. 17. The percentage error between the two is determined by Eq. 13, where X refers to the calculated major strain and X_{exp} to the major strain obtained in the experiments. Table 5 shows a comparison between the major strain experimental results and the values obtained using the analytical method. The percentage error presented by the method proposed in this work varied between 0.1 and 6.7% in the 27 experiments made, indicating good accuracy despite the easy application.

Additionally, we elaborated FFLDs based on Table 5, according to the values obtained using the analytical method. Each FFLD was determined using the angular coefficient -1, and consequently, φ_3 presents constant values under any kind of strain, whereas in the plane state of strain $\varphi_2 = 0$ and in the biaxial stretching state $\varphi_1 = \varphi_2$. Figure 8 shows the minimum and maximum FFLDs for AA1200-H14, SAE1008 and C268, determined by the analytical method developed in this work.

Table 5 Comparison between experimental results and analytical method

| Material	R_t (mm)	σ_c (MPa)	s_0 (mm)	φ_1 exp.(−)	φ_1 calc.(−)	Percentage error (%)
SAE1008	7.5	363.7	0.60	1.192	1.173	1.6
			0.75	1.240	1.225	1.2
			0.90	1.240	1.273	2.7
	5.0	360.3	0.60	1.264	1.234	2.4
			0.75	1.309	1.303	0.5
			0.90	1.331	1.366	2.7
	3.0	342.5	0.60	1.192	1.221	2.4
			0.75	1.331	1.316	1.2
			0.90	1.414	1.401	0.9
AA1200-H14	7.5	104.0	0.50	1.141	1.182	3.6
			0.80	1.373	1.351	1.6
			1.20	1.562	1.534	1.8
	5.0	100.4	0.50	1.141	1.089	4.5
			0.80	1.352	1.305	3.5
			1.20	1.434	1.530	6.7
	3.0	97.4	0.50	1.141	1.161	1.7
			0.80	1.491	1.434	3.8
			1.20	1.674	1.703	1.8
C268	7.5	408.7	0.50	0.906	0.922	1.8
			0.81	1.030	1.015	1.4
			1.06	1.087	1.085	0.2
	5.0	399.2	0.50	0.938	0.930	0.8
			0.81	1.059	1.058	0.1
			1.06	1.141	1.150	0.8
	3.0	352.0	0.50	0.764	0.769	0.6
			0.81	0.970	0.949	2.2
			1.06	1.059	1.075	1.5
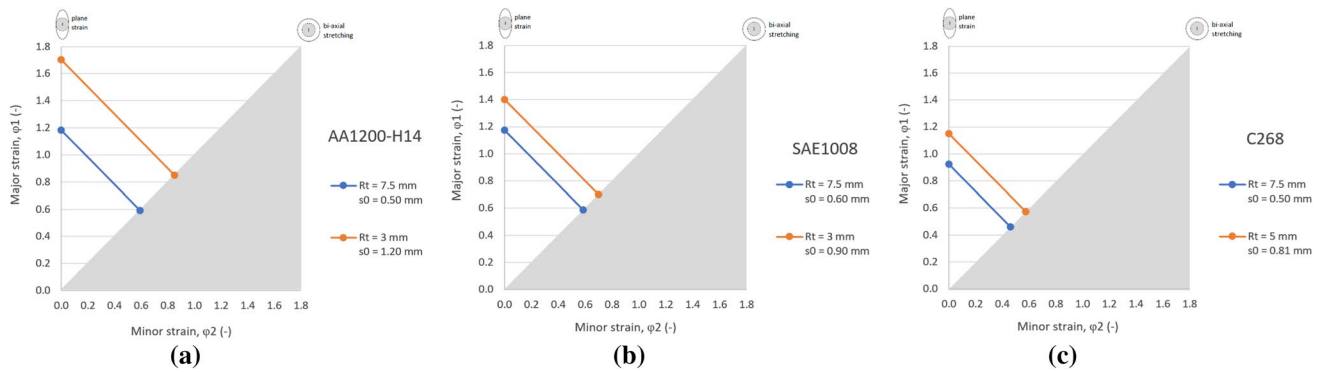
Fig. 8 FFLDs obtained through analytical method for **a** AA1200-H14, **b** SAE1008 and **c** C268

As expected, the largest strain range in FFLD occurred with a smaller radius and greater initial thickness, as shown in Fig. 8a for AA1200-H14 and in Fig. 8b for SAE1008. However, for C268 brass (Fig. 8c), this trend was not met, so that the greatest strain was obtained with a radius of 5 mm and an initial thickness of 0.81 mm. This behavior in C268 is a result of the critical stress corresponding to this material, which for the 5 mm radius is significantly higher than that found for the 3 mm radius, as shown in Fig. 6.

4 Conclusions

In this work, we defined an iterative analytical method to estimate strain limits in SPIF and with them plot the FFLD. After conducting 27 formability experiments in SPIF using different materials, tool radii and initial thicknesses, and conducting subsequent FEM simulations and statistical analysis, it is possible to conclude that:

1. The FEM simulations allowed us to validate the analytical equations for the calculation of principal stress and mean stress according to the membrane equilibrium conditions;
2. The statistical analysis (ANOVA) showed that only the material, the tool radius and the interaction between the two have an effect over critical stress;
3. This study has allowed the definition of a failure criterion for SPIF based on mean stress = critical stress;
4. The iterative method presented in this work allows the estimation of maximum strain, as well as the maximum value of wall angle, and with them plot the FFLD for a determined process condition.

Declarations

Conflict of interest The authors declare no conflicts of interest.

References

1. Chang Z, Li M, Chen J (2019) Analytical modeling and experimental validation of the forming force in several typical incremental sheet forming processes. Int J Mach Tools Manuf 140:62–76. https://doi.org/10.1016/j.ijmachtools.2019.03.003
2. Ai S, Long H (2019) A review on material fracture mechanism in incremental sheet forming. Int J Adv Manuf Technol 104:33–61. https://doi.org/10.1007/s00170-019-03682-6
3. Castelan J, Schaeffer L, Daleffe A et al (2014) Manufacture of custom-made cranial implants from DICOM® images using 3D printing, CAD/CAM technology and incremental sheet forming. Rev Bras Eng Biomed 30:265–273. https://doi.org/10.1590/rbeb.2014.024
4. Ambrogio G, Palumbo G, Sgambitterra E et al (2018) Experimental investigation of the mechanical performances of titanium cranial prostheses manufactured by super plastic forming and single-point incremental forming. Int J Adv Manuf Technol 98:1489–1503. https://doi.org/10.1007/s00170-018-2338-6
5. De Lucca GDS, Ferreira CA, Daleffe A et al (2021) Investigation of photofunctionalization applied to cranial implants produced by incremental sheet forming (ISF). J Mater Res Technol 15:2633–2645. https://doi.org/10.1016/j.jmrt.2021.09.059
6. de Arruda RP, Baroni A, Schaeffer L (2008) Sheet metal forming: new technologies applied to the fabrication of solar energy collector panels. Int J Mechatronics Manuf Syst 1:254–263. https://doi.org/10.1504/IJMMS.2008.02051
7. Schreiber RG, Schaeffer L (2019) Manufacture of absorber fins for solar collector using incremental sheet forming. J Mater Res Technol 8(1):1132–1140. https://doi.org/10.1016/j.jmrt.2018.07.018
8. Schreiber RG, Teixeira AR, Pereira RSF et al (2021) Prototyping of absorber plate for solar collector by ISF and FSW processes. J Brazilian Soc Mech Sci Eng 43:1–12. https://doi.org/10.1007/s40430-021-03083-5
9. Amino M, Mizoguchi M, Terauchi Y, Maki T (2014) Current status of "Dieless" Amino's incremental forming. Procedia Eng 81:54–62. https://doi.org/10.1016/j.proeng.2014.09.128
10. Scheffler S, Pierer A, Scholz P et al (2019) Incremental sheet metal forming on the example of car exterior skin parts. Procedia Manuf 29:105–111. https://doi.org/10.1016/j.promfg.2019.02.112

11. Peter I, Fracchia E, Canale I, Maiorano R (2019) Incremental sheet forming for prototyping automotive modules. Procedia Manuf 32:50–58. https://doi.org/10.1016/j.promfg.2019.02.182

12. Trzepiecinski T, Krasowski B, Kubit A, Wydrzynski D (2018) Possibilities of Application of Incremental Sheet-Forming Technique in Aircraft Industry. Sci Lett Rzesz Univ Technol Mech 87–100

13. Barimani-Varandi A, Nasrabadi MK, Ravan BA, Javadi M (2021) Rapid prototyping of aircraft canopy based on the incremental forming process. J Brazilian Soc Mech Sci Eng 43:1–15. https://doi.org/10.1007/s40430-021-02811-1

14. Do V-C, Pham Q-T, Kim Y-S (2017) Identification of forming limit curve at fracture in incremental sheet forming. Int J Adv Manuf Technol 92:4445–4455. https://doi.org/10.1007/s00170-017-0441-8

15. Khazaali H, Fereshteh-Saniee F (2016) A comprehensive experimental investigation on the influences of the process variables on warm incremental forming of Ti-6Al-4V titanium alloy using a simple technique. Int J Adv Manuf Technol 87:2911–2923. https://doi.org/10.1007/s00170-016-8665-6

16. Khazaali H, Fereshteh-Saniee F (2019) An inclusive experimental investigation on influences of different process parameters in warm incremental forming of AZ31 magnesium sheets. Iran J Sci Technol Trans Mech Eng 43:347–358. https://doi.org/10.1007/s40997-017-0122-0

17. Amini S, Hosseinpour Gollo A, Paktinat H (2016) An investigation of conventional and ultrasonic-assisted incremental forming of annealed AA1050 sheet. Int J Adv Manuf Technol 90:1569–1578. https://doi.org/10.1007/s00170-016-9458-7

18. Behera AK, de Sousa RA, Ingarao G, Oleksik V (2017) Single point incremental forming: an assessment of the progress and technology trends from 2005 to 2015. J Manuf Process 27:37–62. https://doi.org/10.1016/j.jmapro.2017.03.014

19. Pereira Bastos RN, Alves de Sousa RJ, Fernandes Ferreira JA (2016) Enhancing time efficiency on single point incremental forming processes. Int J Mater Form 9:653–662. https://doi.org/10.1007/s12289-015-1251-x

20. Meier H, Magnus C, Smukala V (2011) Impact of superimposed pressure on dieless incremental sheet metal forming with two moving tools. CIRP Ann Manuf Technol 60:327–330. https://doi.org/10.1016/j.cirp.2011.03.134

21. Fang Y, Lu B, Chen J et al (2014) Analytical and experimental investigations on deformation mechanism and fracture behavior in single point incremental forming. J Mater Process Technol 214:1503–1515. https://doi.org/10.1016/j.jmatprotec.2014.02.019

22. Jeswiet J, Micari F, Hirt G et al (2005) Asymmetric single point incremental forming of sheet metal. CIRP Ann Manuf Technol 54:88–114. https://doi.org/10.1016/S0007-8506(07)60021-3

23. Micari F (2004) Single point incremental forming: recent results. In: Seminar on Incremental Forming. Cambridge University

24. Al-Ghamdi KA, Hussain G (2015) Threshold tool-radius condition maximizing the formability in SPIF considering a variety of materials: experimental and FE investigations. Int J Mach Tools Manuf 88:82–94. https://doi.org/10.1016/j.ijmachtools.2014.09.005

25. Gatea S, Ou H, McCartney G (2016) Review on the influence of process parameters in incremental sheet forming. Int J Adv Manuf Technol 87:479–499. https://doi.org/10.1007/s00170-016-8426-6

26. Martins PAF, Bay N, Skjoedt M, Silva MB (2008) Theory of single point incremental forming. CIRP Ann Manuf Technol 57:247–252. https://doi.org/10.1016/j.cirp.2008.03.047

27. Gatea S, Lu B, Chen J et al (2019) Investigation of the effect of forming parameters in incremental sheet forming using a micromechanics based damage model. Int J Mater Form 12:553–574. https://doi.org/10.1007/s12289-018-1434-3

28. Han HN, Kim KH (2003) A ductile fracture criterion in sheet metal forming process. J Mater Process Technol 142:231–238. https://doi.org/10.1016/S0924-0136(03)00587-9

29. Huang Y, Smith S, Ziegert J, et al (2009) Studies of size effect on the formability of a domed part in incremental forming. Proc ASME Int Manuf Sci Eng Conf MSEC2008 1:645–654. https://doi.org/10.1115/MSEC_ICMP2008-72545

30. Silva MB, Skjoedr M, Atkins AG et al (2008) Single-point incremental forming and formability-failure diagrams. J Strain Anal Eng Des 43:15–35. https://doi.org/10.1243/03093247JSA340

31. Wu R, Hu Q, Li M et al (2021) Evaluation of the forming limit of incremental sheet forming based on ductile damage. J Mater Process Technol. https://doi.org/10.1016/j.jmatprotec.2019.116497

32. Haag J, Ferranti GO (2017) Estampabilidade De Aços De Baixo Carbono. 54° Semin Laminação e Conform 54:308–319. https://doi.org/10.5151/1983-4764-30515

33. Maximiliano G, Schaeffer L, Daleffe A, et al (2016) Estampagem Incremental de Múltiplos Passes em Chapa de Latão C268. 36° SENAFOR /19ª Conferência Nac Conform Chapas/6ª Conferência Int Conform Chapas /3° Congr do BrDDRG

34. Bhattacharya A, Maneesh K, Reddy NV, Cao J (2011) Formability and surface finish studies in single point incremental forming. J Manuf Sci Eng. https://doi.org/10.1115/1.40054.58

35. Jalali A, Hashemi R, Rajabi M, Tayebi P (2021) Finite element simulations and experimental verifications for forming limit curve determination of two-layer aluminum/brass sheets considering the incremental forming process. Proc Inst Mech Eng Part L J Mater Des Appl 236:361–373. https://doi.org/10.1177/14644207211045212

36. Tayebi P, Fazli A, Asadi P, Soltanpour M (2019) Formability analysis of dissimilar friction stir welded AA 6061 and AA 5083 blanks by SPIF process. CIRP J Manuf Sci Technol 25:50–68. https://doi.org/10.1016/j.cirpj.2019.02.002